2024-01-01

Fabrication of porous carbon nanofiber webs from polyacrylonitrile and cellulose acetate for NaCl removal from water using capacitive deionization

Tarus, Bethwel

IWA Publishing

Water Supply

Water Supply Vol 24 No 1, 39 doi: 10.2166/ws.2023.334

Fabrication of porous carbon nanofiber webs from polyacrylonitrile and cellulose acetate for NaCl removal from water using capacitive deionization

Bethwel Tarus[a], Yusufu Jande[b,*] and Karoli Njau[c]

[a] Department of Materials and Energy Science and Engineering, Nelson Mandela African Institution of Science and Technology, P.O. Box 447, Arusha, Tanzania
[b] Water Infrastructure and Sustainable Energy Futures (WISE-Futures), African Centre of Excellence, Nelson Mandela African Institution of Science and Technology, Nelson Mandela Road, Tengeru, P.O. Box 9124, Arusha, Tanzania
[c] Department of Water and Environmental Science and Engineering, Nelson Mandela African Institution of Science and Technology, P.O. Box 447, Arusha, Tanzania
*Corresponding author. E-mail: yusufu.jande@nm-aist.ac.tz

ABSTRACT

Capacitive deionization (CDI) has shown potential in addressing freshwater scarcity. CDI's electrode design is a key to better performance as it determines the extent of water purification. For carbon electrodes, the pore structure is an important factor influencing removal kinetics and ion storage. Herein, porous carbon nanofibers with diameters ranging from 277 to 348 nm were fabricated from blends of polyacrylonitrile (PAN) and cellulose acetate (CA) through electrospinning and carbonization. Surface area and pore properties were adjusted by varying the proportions of the precursors while ensuring no adverse alteration to the products' tangible properties. Enhanced pore structure and specific surface area were evident in the blend-based carbon nanofibers. The blend ratio of 2:8 (CA:PAN) had a high specific surface area of 925.47 m^2/g and a pore volume of 0.7884 cm^3/g. Correspondingly, a high specific capacitance of 177.5 F/g was attained. Desalination performance was determined in batch mode using 500 mg/L NaCl solution. A salt adsorption capacity of 6.57 mg/g and charge efficiency of 0.46 was obtained for the blend that had 20% CA. The carbon nanofibers demonstrated good desalination stability when used repetitively indicating their excellent potential for practical application.

Key words: capacitive deionization, carbon nanofibers, desalination, electrosorption, electrospinning

HIGHLIGHTS

- Carbon nanofibers with a hierarchical micro/mesoporous structure and high surface area were fabricated.
- Cellulose acetate was used as a green sacrificial porogen in porous carbon fabrication.
- A blend of polyacrylonitrile and cellulose acetate resulted in carbon nanofibers with high ionic transport and charge transfer performance.
- A desalination capacity of 6.57 mg/g and charge efficiency of 0.46 was achieved.

GRAPHICAL ABSTRACT

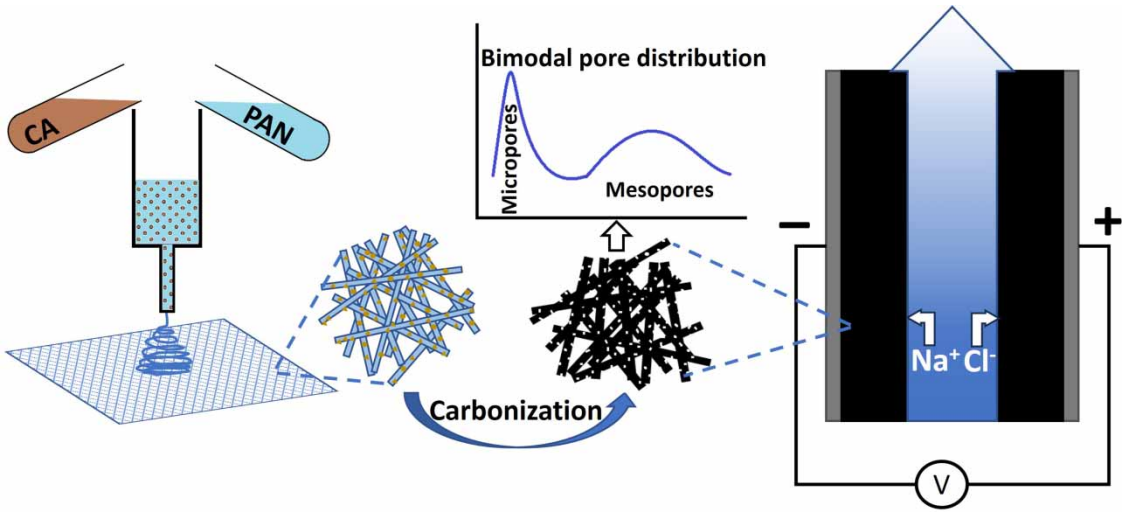

INTRODUCTION

Freshwater is an important resource for domestic, industrial, and agricultural uses. The global demand for fresh water has exceeded supply due to rapid population growth, industrialization, and the effects of climate change. To meet the pressing shortage, various methods such as reverse osmosis (Voutchkov 2018; Qasim *et al.* 2019), thermal distillation (Brogioli *et al.* 2018), and electrodialysis (Al-Amshawee *et al.* 2020) have been successfully used to extract fresh water from nonconventional sources including wastewater, seawater, or underground brackish/saline waters, which are vast but minimally exploited (Ahdab *et al.* 2018). However, these methods are hampered by high energy requirements and/or costly maintenance that renders them expensive for desalination of moderately saline waters (Liu *et al.* 2021; Tong *et al.* 2021). Relatively new techniques such as capacitive deionization (CDI) have gained substantial research interest with much promise for fresh water production from moderately saline sources at reasonable energy requirements (Suss *et al.* 2015). The conventional CDI process is based on the electric double layer (EDL) where there is electrosorption of ions onto the surfaces of charged porous electrodes. An electric field is applied between the electrodes to cause ions to be attracted and immobilized in the pores of the electrode possessing an opposite charge (Ahmed & Tewari 2018). The electrodes are regenerated by short circuiting or reversing the applied potential resulting in the release of a concentrated salt stream (Porada *et al.* 2013). When a reversed potential is applied to regenerate the electrodes, it is recommended to use ion exchange membranes to achieve better control of the discharge process and prevent possible shift of ions from one electrode to the other (Porada *et al.* 2012, 2013). The electrosorptive capacity of CDI electrodes is determined by their pore structure, pore size distribution, accessible surface area, and availability of functional groups (Liu *et al.* 2016). Certainly, the electrode materials are a major factor in the performance of CDI (Peng *et al.* 2020). Typical materials that have been used include graphene (Zhang *et al.* 2019), carbon aerogel (Liu *et al.* 2019), carbon cloth (Myint & Dutta 2012), carbon nanotubes (Nie *et al.* 2012), different forms of activated carbon (Alfredy *et al.* 2019; Elisadiki *et al.* 2020), carbide-derived carbons (Porada *et al.* 2012), carbon nanofibers (Nie *et al.* 2021). These materials possess sufficiently high specific surface area, excellent electrical conductivity, and good chemical stability, and their different routes of production allow tailoring of their functional properties (Pan *et al.* 2015). Control of the porosities of these materials is an important aspect during their fabrication. A hierarchical structure with a uniform distribution of micropores (<2 nm) and mesopores (2–50 nm) enhances performance in CDI (Wang *et al.* 2016).

Electrospinning is a simple and robust nanofiber fabrication method that allows for a high degree of control of the nanofiber's functional properties (Xue *et al.* 2019). Electrospun carbon nanofibers have had significant interests in many applications including sensors, energy storage, and catalysis (Zhang *et al.* 2014). Their attractiveness to electrochemical applications is due to their exceptional properties such as high surface area, tunable porosity, good electrical conductivity, and freestanding nature without the use of binders (Zhang *et al.* 2016). A popular precursor for electrospun carbon nanofibers is polyacrylonitrile (PAN), which has a high carbon yield and a molecular structure suitable for fiber formation (Nataraj

et al. 2012; Tarus *et al.* 2022). Its chemical structure is very robust endowing it with good chemical resistance, thermal stability, and excellent mechanical properties (Bai *et al.* 2022). However, PAN-based carbon nanofibers possess significant microporosity, which is disadvantageous to the electrosorption of ions in CDI. Micropores may become trap sites and increase ion transfer resistance, thus diminishing desalination performance (Wang *et al.* 2016). It then becomes necessary to develop carbon nanofibers having a hierarchical pore structure with well-distributed and interconnected micropores and mesopores. Chemical and physical activation are sound ways of enhancing pore properties and surface area but may result in lower yields, have lengthy durations for activation, and require high activation temperatures, and the products may need significant washing to remove residual chemicals (Kim *et al.* 2017; Yin *et al.* 2020). The use of porogens/sacrificial components is a simpler and more straightforward way of enhancing carbon nanofibers' pore characteristics (Ma *et al.* 2021). A sacrificial constituent that gets removed in later processes is added to the precursor solution to create mesopores in the carbon nanofibers. Blending PAN with sacrificial polymers such as polymethyl methacrylate (PMMA) (El-Deen *et al.* 2013; Liu *et al.* 2016), polyvinyl pyrrolidone (PVP) (Wang *et al.* 2016), and polystyrene (Liu *et al.* 2016) has yielded carbon nanofibers with varying but enhanced mesoporosity. Different levels of porosities are possible by varying the proportions of the additives. The type of porogen used is also important as it determines the possible type and size of pores that are formed (Liu *et al.* 2016; Ghosh *et al.* 2019; Yan *et al.* 2021). For polymers, the solubility parameter of the particular polymers used in the blend is a critical factor. The sizes of the pores created increase with the increase in the difference in the solubility parameters of the blended polymers (Jo *et al.* 2014).

However, the sacrificial nature of pore templates can become a problem environmentally and economically. From many studies, it is noticed that the pore agents used are wholly synthetic, which raises queries regarding their sustainability. Obviously, the use of green sacrificial agents offers many advantages, but there is a need to evaluate their effects on electrode structure and performance. Herein, a precursor blend of PAN and cellulose acetate (CA) is evaluated for porous carbon nanofiber fabrication. Even though the two precursors are carbonizing polymers, CA is degradable at relatively low temperatures (Erdmann *et al.* 2021) with a low carbon yield (barely 11%) and can work as a pore agent as well as contribute to the fiber yield (Donnet *et al.* 2003). The immiscibility of the two polymers in solution (Kim *et al.* 2000) and their different thermal properties help in creating a unique pore structure during carbonization (Ju *et al.* 2009). Importantly, CA is a regenerated polymer obtained from cellulose, which is largely abundant and renewable, and its use as a sacrificial agent is economically sensible. As a green polymer, it has been extensively used to fabricate nanofibers through electrospinning for a wide range of applications and particularly those requiring high sorption performance (Feng *et al.* 2018; Khodayari *et al.* 2022). The good physicochemical properties of CA also help to enhance the fabrication of other materials via electrospinning (Phan *et al.* 2019).

In this study, porous carbon nanofibers were fabricated through electrospinning and carbonization of a blend of CA and PAN at varying proportions. With PAN as the principal carbon precursor, gradual increments of CA proportion in the dope solution were made to determine the highest proportion of CA dosage to fabricate carbon nanofibers with a good pore structure while maintaining good mechanical integrity. Thermal gravimetric analysis (TGA) and Fourier transform infrared (FT-IR) spectroscopy were used to highlight the structural evolution of the nanofibers during processing. The morphologies and pore properties of the obtained carbon nanofibers were analyzed using scanning electron microscopy (SEM) and nitrogen sorption isotherms. The electrochemical properties and the desalination performance of the produced carbon nanofibers were discussed with emphasis on the effect of pore structure as a consequence of adding varying CA proportions.

MATERIALS AND METHODS

Materials

PAN (Mw = 150,000), CA (Mw = 30,000) having acetylation content of 39.8%, and *N*,*N*-dimethyl formamide (DMF) (>99.8%) were purchased from Sigma Aldrich, USA. All chemicals were analytical grade and were used without further purification.

Fabrication of carbon nanofibers

The electrospinning solutions were prepared at a polymer concentration of 10 wt.% in DMF. The CA:PAN blend ratios were 10:90, 20:80, 30:70, and 40:60 by mass. A pure PAN solution was also prepared for control samples. To prepare the solutions, a total of 1.12 g of PAN and CA were dissolved in 10 g DMF under continuous stirring at 50 °C for 6 h to achieve homogeneity. Subsequently, the polymer solutions were drawn into a 10 mL syringe having a stainless steel blunt-ended needle with

0.8 mm internal diameter. A high DC voltage power supply (DW-P303–1ACD1, Dongwen High Voltage, China) was used to deliver the required charge to the solution during the process. Electrospun nanofibers were collected on an aluminum foil covering a stationary flat stage. The electrospinning process was carried out at a voltage of 15 kV, a solution flowrate of 1 mL/h, and a collection height of 15 cm. The electrospinning setup had a vertical configuration as shown in Figure S1.

The as-obtained nanofibers were stabilized in a muffle furnace by heating at a rate of 2 °C/min in air and holding at 260 °C for 60 min. The stabilized nanofibers were denoted as SNF, SNF-1:9, SNF-2:8, SNF-3:7, and SNF-4:6 corresponding to CA: PAN ratios of 0:100, 10:90, 20:80, 30:70, and 40:60, respectively. The stabilized nanofibers were then carbonized in a tube furnace by heating at 5 °C/min to a temperature of 800 °C, which was held for 60 mins before cooling. The whole carbonization process was under continuous nitrogen flow at 100 cc/min. The carbon nanofibers obtained from pure PAN were denoted as CNF, while those obtained from the CA:PAN blends (10:90, 20:80, 30:70 and 40:60) were denoted as CNF-1:9, CNF-2:8, CNF-3:7, and CNF-4:6 accordingly.

Characterizations

The morphology and diameters of the nanofibers were evaluated using a field emission scanning electron microscope (FE-SEM; SU8200). Fiber diameters were analyzed from the FE-SEM micrographs using ImageJ (image analysis software). TGA tests were carried out on a thermogravimetric analyzer (Q600 SDT) under a nitrogen environment. The pore characteristics and the Brunauer–Emmett–Teller (BET) specific surface area of the carbonized nanofibers were evaluated from nitrogen adsorption/desorption isotherms at 77 K (Autosorb-iQ, Quantachrome Instruments, USA). Pore size distributions were determined using the Barrett–Joyner–Halenda (BJH) method.

Electrochemical measurements

Electrochemical impedance spectroscopy (EIS) and cyclic voltammetry (CV) measurements were performed using an Autolab potentiostat/galvanostat (PGSTAT204, Metrohm) in 6 M KOH solution using a three-electrode system consisting of a working electrode, reference electrode (Ag/AgCl), and a platinum wire counter electrode at scan rates of 5, 10, 20, 50, and 100 mV/s. The working electrodes were prepared from individual carbon nanofiber sheets cut into 10 mm × 10 mm samples. EIS was carried out at a frequency range of 10 kHz–1 mHz and an amplitude of 5 mV. The specific capacitance (C_s) (F/g) was determined from the CV curves using Equation (1).

$$C_S = \frac{Q}{2 \cdot v \cdot \Delta U \cdot m} \tag{1}$$

where Q is the integral area of the CV curves, v is the scan rate (V/s), ΔU is the voltage window (V), and m is the mass (g) of the electrode.

Capacitive deionization experiments

The CDI cell was of square construction with an effective chamber of 40 mm × 40 mm consisting of carbon nanofiber electrodes, current collectors, silicone gaskets, and a fabric spacer as shown in Figure S3. A schematic of the desalination setup is shown in Figure 1.

Before assembling in a CDI cell, the electrodes were soaked in 500 mg/L NaCl solution for physical adsorption equilibrium to occur. Electrosorption experiments were then carried out in batch mode (Figure 1) by continuously circulating 50 mL NaCl solution with a concentration of 500 mg/L through the cell using a peristaltic pump (Masterflex, L/S series, USA) at a flow rate of 5 mL/min. Charging and discharging of the cell were done using a potentiostat/galvanostat (Vertex, Ivium Technologies, the Netherlands). A charging voltage of 1.2 V was applied, while discharging was by short circuit (0 V). A change in solution conductivity was continuously monitored and recorded using a multiparameter meter (Orion Versa Star Pro, Thermo Scientific, USA) at 5-s time intervals. The electrosorption capacity (D) (mg/g) and charge efficiency (Λ) of the electrodes were calculated using Equations (2) and (3), respectively.

$$D = \frac{(C_O - C) \cdot V}{m} \tag{2}$$

$$\Lambda = \frac{m \cdot D \cdot F}{1000 \cdot M \cdot \int i \cdot dt} \tag{3}$$

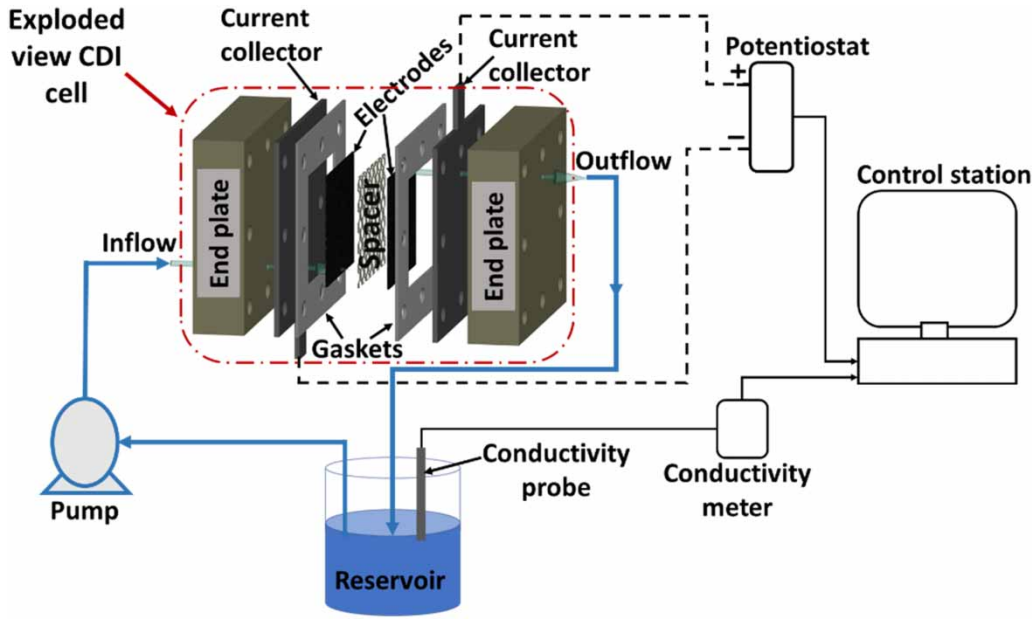

Figure 1 | Representation of the CDI desalination setup.

where C_O and C are the initial and final salt concentrations (mg/L), respectively, V is the volume of the solution (L), m is the total mass (g) of the electrodes, F is the Faraday's constant (mol/C), M is the molar mass of NaCl (g/mol), i is the current (A), and t is the charging time (s).

RESULTS AND DISCUSSION

Nanofiber morphology

The general appearances of the as-spun, stabilized, and carbonized nanofiber sheets are shown in Figure S2. All the obtained nanofiber webs collected on the aluminum foil had a white color. The thermal treatment conditions applied for the nanofibers, i.e., heating rates and stabilization temperature were based on reported optimized conditions for PAN-based nanofibers (Barua & Saha 2018). The stabilized nanofiber sheets had a deep brown color for all the samples. After the carbonization step, the sheets attained a black color. The texture of the thermally treated nanofiber sheets varied with changes in the amount of CA content. SNF, SNF-1:9, and SNF-2:8 (Figures 2(a)–2(c)) exhibited a soft feel and were very easy to fold without damage. On the other hand, SNF-3:7 and SNF-4:6 were less soft with lower flexibility and cracked easily as shown in Figures 2(d) and 2(e), respectively. However, with careful handling, they could be prepared for the carbonization process. For the carbonized nanofibers, CNF, CNF-1:9, and CNF-2:8 (Figures 2(f)–2(h)) had uniform smooth surfaces with moderate flexibility and could be readily prepared into electrodes. CNF-3:7 (Figure 2(i)) had poor flexibility and cracked easily but could be handled and prepared into free-standing electrodes. As shown in Figure 2(j), CNF-4:6 was very fragile and had cracks upon removal from the furnace and could not be prepared for further tests while maintaining the free-standing form. The different thermal properties of CA and PAN are the major cause of the change in the physical properties of the thermally processed nanofiber sheets. The softening point of CA is lower than the temperature that was required for the stabilization of the nanofibers. CA cannot be directly carbonized while maintaining its fibrous form as it undergoes melting when heated above its softening temperature (Ganster & Fink 2013; Fan *et al.* 2019). Thus, during stabilization, phase separation occurred as the CA softened within the continuous phase of PAN. It is thought that at relatively high CA proportions, excessive separation occurred leading to unbalanced tensions and the creation of weak spots in the samples. These effects would become magnified in the carbonized nanofibers as was observed for CNF-3:7 and CNF-4:6. Wang *et al.* (2020) concluded that the thermal properties of a composite nanofiber network were determined by the inherent properties of the individual constituents.

As determined from FE-SEM micrographs, the diameters of uncarbonized nanofibers ranged between 516 and 596 nm. Nanofiber diameter increased with the addition and increase of the CA content. The increase in diameter was mainly due

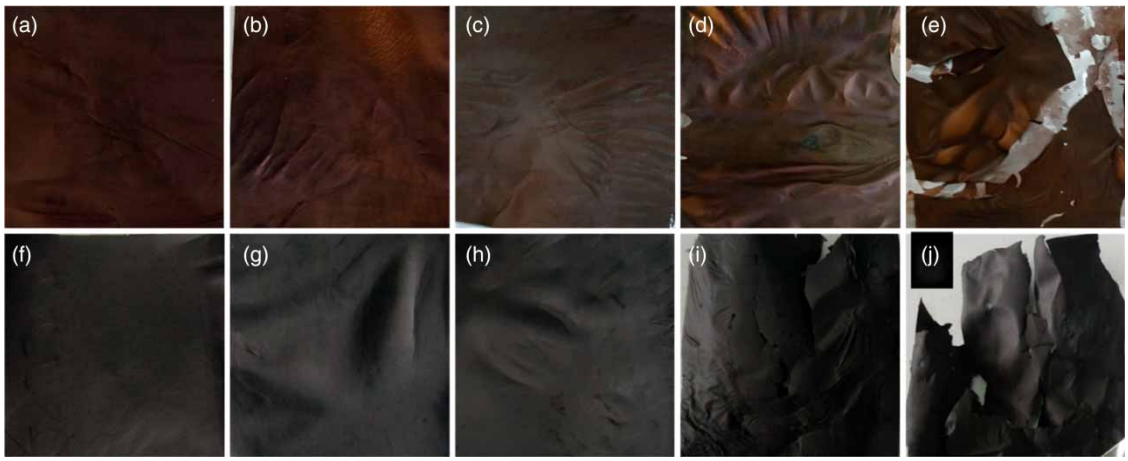

Figure 2 | (a–e) Stabilized nanofiber sheets: (a) SNF, (b) SNF-1:9, (c) SNF-2:8, (d) SNF-3:7, (e) SNF-4:6, and (f–j) carbonized nanofiber sheets; (f) CNF, (g) CNF-1:9, (h) CNF-2:8, (i) CNF-3:7, and (j) CNF-4:6.

to increased solution viscosity as there were more polymer chain interactions within the blend caused by the spirally shaped molecule chains of CA (Wu *et al.* 2015). The diameters of the nanofibers reduced after stabilization and carbonization due to evaporation of residual solvents and heteroatom removal (Zhang *et al.* 2016). The average diameters of the carbonized nanofibers ranged between 277 and 348 nm. Other than the dimension changes, the surfaces of pure PAN carbonized nanofibers were uniform and unaltered by the thermal treatments (Figure 3(a)). The nanofiber surfaces appear smooth with no obvious indication of induced porosity. For the blends, however, fiber bends, creases/channels, and broken ends are noticed after carbonization. The nanofiber bends and creases increased with the increasing CA content. In addition, high CA content caused the fibers to appear to adhere to each other and flatten at contact points (Figure 3(c)). This is a prominent feature in CNF-3:7, which is likely linked to its relatively low surface area and desalination performance (*vide infra*). The bends and creases of the blend-based carbon nanofibers can be attributed to the effects of phase separation (Jo *et al.* 2014) and the different thermal stabilities of CA and PAN causing the nanofiber matrix to undergo uneven tensions during heating. The fiber fusions and flattening at junction points for the high CA blends can be attributed to the melting temperature of CA (230–250 °C) (Erdmann *et al.* 2021), which is below the stabilization temperature used. As shown in Figure 3(b), CNF-2:8 shows continuous channels along the fiber length and within its structure. It is also evident that there is an interconnection between the outer and inner channels, which is highly favorable for ionic transportation. As for CNF-3:7, it is quite probable that such interconnections are lost or reduced when fiber fusing and flattening occurs.

Thermogravimetric analysis

Thermogravimetric experiments were carried out to analyze the pyrolysis characteristics of the electrospun nanofibers. A slight initial weight loss for all the samples was observed below 200 °C due to moisture and residual solvent evaporation.

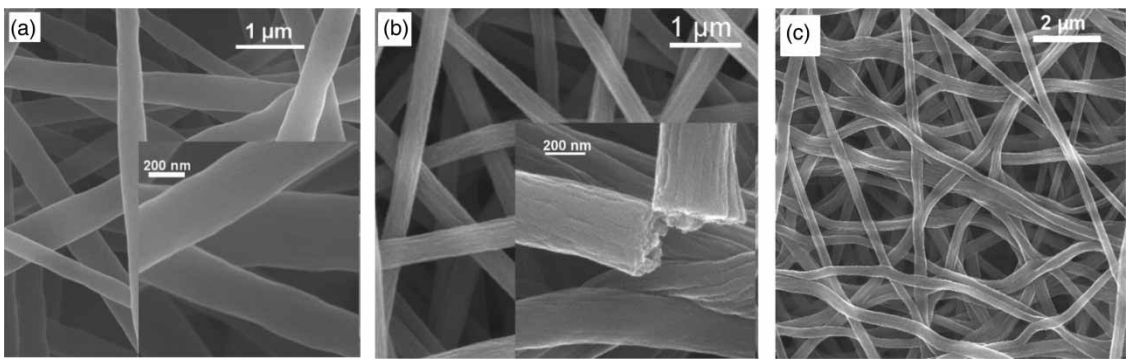

Figure 3 | FE-SEM images of (a) CNF, (b) CNF-2:8, and (c) CNF-3:7.

A degradation process at two different rates was observed for PAN as shown in Figure 4(a). The first was a rapid mass loss which occurred between ~275 and ~300 °C. The second stage was at a lower mass loss rate and occurred between ~300 and ~500 °C. The first rapid degradation step has been attributed to cyclization and dehydrogenation reactions accompanied by the evolution of pyrolytic gases. The slower rate of degradation is attributable to the elimination of small oxygen-containing groups (Wu *et al.* 2015; Dadol *et al.* 2020). A one-step mass loss process was observed for CA that occurred from ~280 to ~400 °C. Mass loss in CA occurred due to dehydration, deacetylation, and the formation of volatiles (Gaan *et al.* 2011; Dadol *et al.* 2020). A total mass loss of about 60% was observed for PAN. Mass loss in CA was higher at about 89%, while the CA/PAN blend at a ratio of 30:70 lost about 67% of its mass at 800 °C. Further studies have been proposed to investigate the interaction between CA and PAN during carbonization (Wu *et al.* 2015).

FT-IR analysis

The FT-IR spectra of the uncarbonized and carbonized nanofibers are shown in Figure 4. From Figure 4(b), the characteristic peaks of PAN at 2,936 cm^{-1}, 2,244 cm^{-1}, and 1,451 cm^{-1} corresponding to stretching vibrations of the C – H and C ≡ N bonds and C–H in-plane deformation vibrations, respectively, are maintained in the CA/PAN blend (Wang *et al.* 2020). The peak at 1,233 cm^{-1} characterizing the C–O–C antisymmetric stretch vibrations of the ester groups and the band at 1,747 cm^{-1} attributed to the C = O bonds in CA are all maintained in the blend (Wu *et al.* 2015). This indicates that only physical blending occurred and the presence of either polymer in the blend does not affect their molecular structures. After the stabilization and carbonization processes, the nanofibers' structure had been significantly changed as indicated by the disappearance of characteristic absorption peaks associated with either polymer as shown in Figure 4(c). The spectra of carbonized nanofibers from pure PAN and from the blend of CA and PAN show similar absorption peaks at 1,558 cm^{-1} and 1,205 cm^{-1}, which can be attributed to the stretching and bending vibrations of N–H/C = C and –C–C bonds, respectively (Kumar *et al.* 2007; Xu *et al.* 2020). Very weak absorption peaks associated with C–N, C = N, and C–H could still be found on the spectra, indicating that not all the heteroatomic rings were converted. The presence of heteroatoms in CDI electrodes has

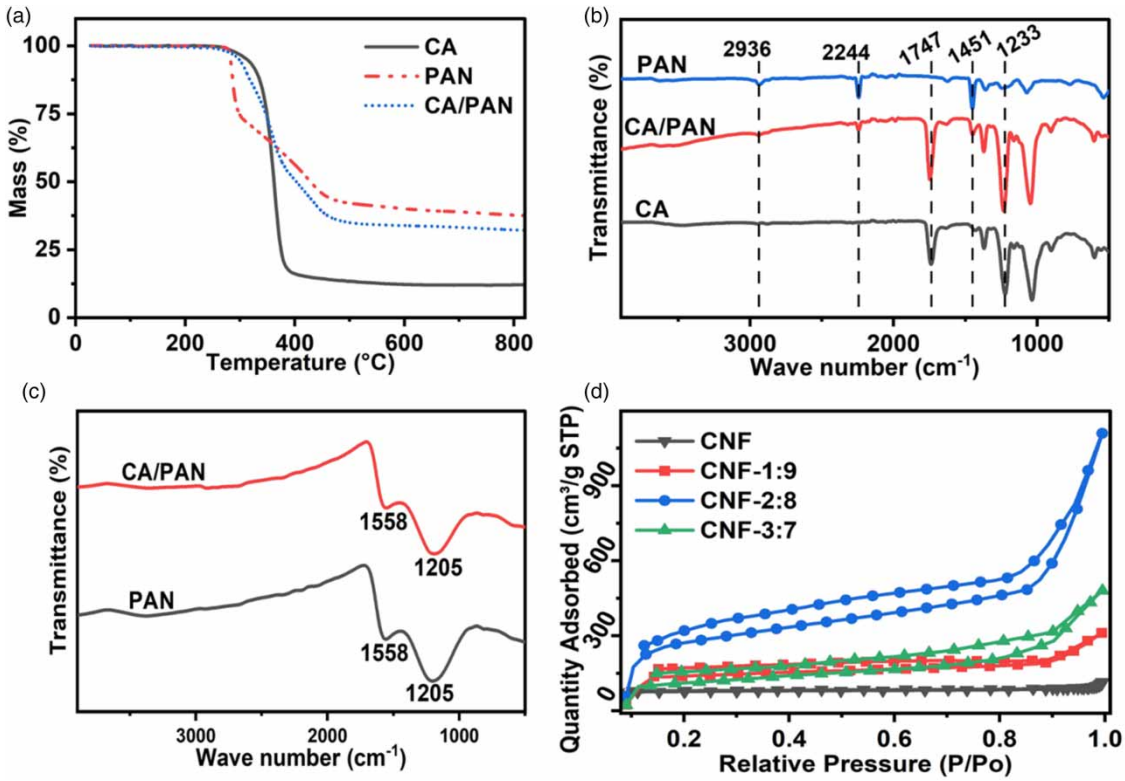

Figure 4 | (a) Thermogravimetric curves of CA, PAN, and CA/PAN blended nanofibers; (b) FT-IR spectra of CA, PAN, and CA/PAN blended nanofibers; (c) FT-IR spectra of the carbonized PAN and CA/PAN blend; (d) nitrogen adsorption/desorption isotherms of CNF, CNF-1:9, CNF-2:8, and CNF-3:7.

been shown to enhance electrochemical performance by increasing the hydrophilicity and electronic conductivity of the electrodes (Kim *et al.* 2020).

Nitrogen sorption analysis

For carbon-based electrodes to have excellent EDL characteristics, they must possess sufficient surface area and good pore distribution. Nitrogen sorption tests were performed to determine the pore characteristics and specific surface area of the nanofibers. Figure 4(d) shows the adsorption/desorption isotherms of the carbon nanofibers at different polymer ratios. The isotherm of CNF depicted a typical microporous material with low nitrogen uptake signifying its low pore volume (Cychosz & Thommes 2018). All the blend-based carbon nanofibers exhibited a hysteresis loop (typical type-IV isotherms) signifying relatively high surface area and the coexistence of micropores and mesopores (Ju *et al.* 2009; Ghosh *et al.* 2019). Table 1 summarizes the BET-specific surface area, pore volume, and the average pore diameter of the carbon nanofibers. Generally, surface area and pore volume were in the order CNF-2:8 > CNF-3:7 > CNF-1:9 > CNF. The high surface area in CNF-2:8 (925.47 m^2/g) was mainly due to the interconnected channels along the nanofiber axis allowing access to inner pores. This is a key to better formation of the EDL and rapid surface kinetics, hence enhancing electrosorption during desalination. The reduced surface area at a high CA amount can be attributed to the flattened and fused nanofibers as observed in the SEM images of CNF-3:7 (Figure 3(c)), which deterred accessibility of inner pores. Pore blockage due to increased residual CA-based char and enlargement and merging of mesopores during carbonization could also have contributed to the reduced surface area (Lee *et al.* 2015). It is worth noting that the average pore diameters of all the blend-based carbon nanofibers fall under mesopore classification (2–50 nm), while the pure PAN-based sample is classifiable as microporous (<2 nm). As shown in Figure 5, CNF-1:9, CNF-2:8, and CNF-3:7 exhibit bimodal pore size distributions up to 50 nm signifying well-distributed pore sizes in the micropore and mesopore regions and thus possess hierarchical structures necessary for enhanced ionic transportation in CDI.

Table 1 | Pore properties of the electrospun carbon nanofibers

Sample	BET surface area (m^2/g)	Pore volume (cm^3/g)	Average pore diameter (nm)
CNF	243.17	0.0957	1.574
CNF-1:9	325.83	0.2091	2.567
CNF-2:8	925.47	0.7884	3.407
CNF-3:7	383.76	0.7511	7.829

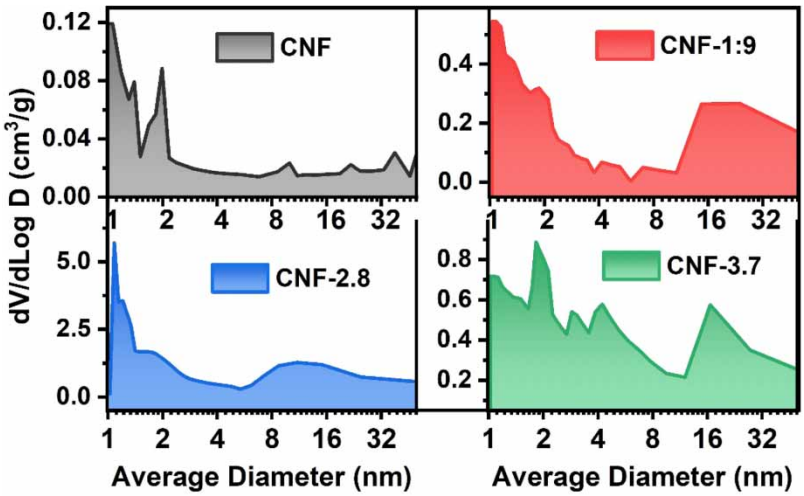

Figure 5 | BJH pore size distribution plots of CNF, CNF-1:9, CNF-2:8, and CNF-3:7.

Electrochemical characterization

Figure 6(a) shows the CV plots of the carbon nanofibers at different CA ratios at a scan rate of 5 mV/s. The CV curves exhibit a quasi-rectangular shape, indicating typical capacitive action. This behavior was certainly due to the presence of pores in the nanofibers, which facilitated the diffusion and transportation of ions (García-Mateos *et al.* 2020). The capacitive current is observed to increase as the CA proportion is increased up to 20% and then decreases for the higher CA content. The low current in CNF was mainly because of the low specific surface area and lack of mesopores as observed from the BJH pore size distribution plots. Figure 6(b) shows the specific capacitance values calculated from the CV curves in relation to the blend ratios and are seen to vary correspondingly to the specific surface area. An increase in capacitance with the increasing specific surface area has been attributed to the availability of more channels and electrosorption sites for diffusion, transfer, and storage of ions (Zhang *et al.* 2019). Figure 6(c) shows the CV curves of CNF-2:8 at varying scan rates (5–100) mV/s. As expected, it is observed that the charge/discharge current increased as the scan rate was increased. The curves also maintain a quasi-rectangular shape (EDL behavior) even at a large scan rate implying improved rate characteristics (Wang *et al.* 2016). The specific capacitances at each scan rate for the different blend ratios (Figure 6(d)) decreased with an increase in the scan rate. This occurred since at rapid scan rates, sufficient time is not provided to enable diffusion of the ions into the deeper pores (Liu *et al.* 2016; Zhang *et al.* 2019).

Impedance spectroscopy (EIS) was performed to evaluate the charge transfer and ionic conductivity characteristics of the carbon nanofibers. Figure 7 shows the Nyquist plots of the carbon nanofibers at a frequency range of 100–10 mHz. The size of the semicircle in the high-frequency region gives information regarding charge transfer resistance at the interface of the electrode and the electrolyte as well as the mobility of the ions at the electrode surface. A small semicircle indicates better accessibility and shorter ion diffusion paths (Liu *et al.* 2016; Ekabutr *et al.* 2018). The electrochemical activity and morphological properties of the electrode materials strongly influence these characteristics (Kim *et al.* 2020). The straight-line slope in the low-frequency region characterizes the ionic diffusion process. A steep slope tending toward the imaginary resistance

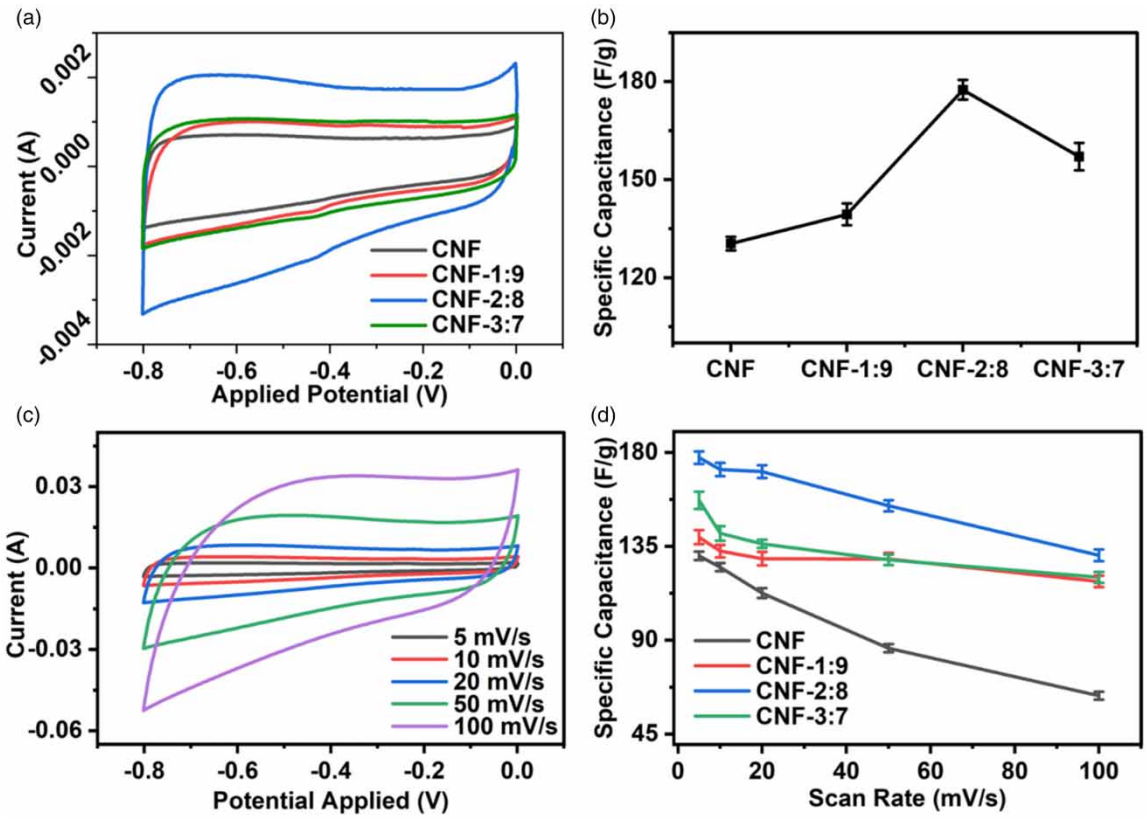

Figure 6 | (a) CV curves and (b) the specific capacitance of CNF, CNF-1:9, CNF-2:8, and CNF-3:7 at a scan rate of 5 mV/s; (c) CV curves of CNF-2:8 at different scan rates; and (d) specific capacitance of the different electrodes at varying scan rates.

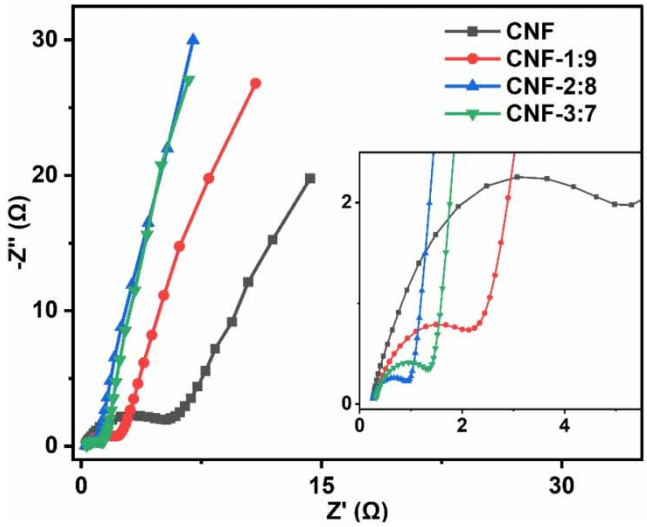

Figure 7 | Nyquist plots of CNF, CNF-1:9, CNF-2:8, and CNF-3:7.

(-Z”)-axis indicates better ionic diffusion. From the Nyquist plots (inset) in Figure 7, it is noted that the sizes of the semicircles in the high-frequency region reduced significantly with the presence of CA. This indicated that charge transfer resistance was high for unblended carbon nanofibers and decreased with an increase in CA amount to reach the lowest for CNF-2:8. The improvement in charge transfer resistance was mainly due to the increased specific surface area, improved pore structure, and rougher surfaces of the carbon nanofibers with the increasing CA content. The blended carbon nanofibers exhibited better ionic diffusion than the unblended ones as indicated by the slopes of the plots at the low-frequency region. The plots for the blended carbon nanofibers tended more toward the -Z”-axis, as compared to the unblended carbon nanofibers implying easier ionic diffusion and appropriateness for CDI application.

Desalination measurements

Upon application of a potential to the CDI cell, ions present in the solution were adsorbed into the electrode pores and the conductivity of the water started to decrease accordingly as shown in Figure 8(a). The initial drop in conductivity for all the samples was quite rapid. It then started to slow down and reached a constant level, indicating that the electrodes were saturated and could not adsorb more ions. For all the samples, constant conductivity was reached in less than 25 min. The extent

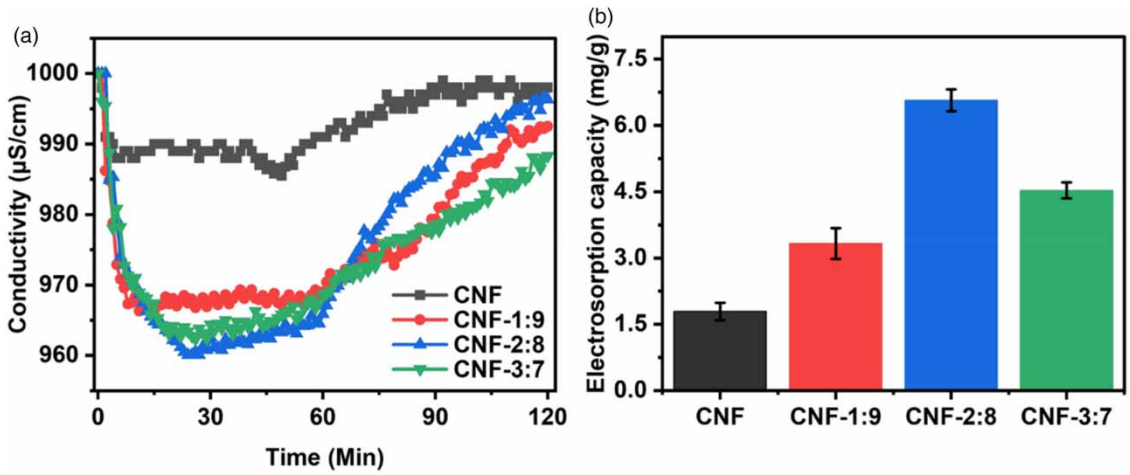

Figure 8 | (a) Change in solution conductivity with time during the desalination process for the electrode samples and (b) electrosorption capacity of the carbon nanofibers at different blend ratios.

of ion removal for all the blend-based carbon nanofibers was significantly larger when compared to the pure PAN-based sample. This is attributable to the micro–mesoporous structure of the blends that allowed for rapid and easy transport of ions. On the other hand, the highly microporous structure of CNF resulted in the blocking of ions and overlapping of the EDL, which occurs when the pore size is similar to EDL thickness (Shui & Alhseinat 2020). Upon discharging the CDI cell, water conductivity started to increase gradually due to desorption of ions from the electrodes. As shown in Figure 8(b), the calculated electrosorption capacity was the lowest for the unblended carbon nanofiber electrodes. It was the highest for the CNF-2:8 electrode, which had a capacity of 6.57 mg/g, consistent with the CV performance and the BET-specific surface area results. The electrodes from CNF, CNF-1:9, and CNF-3:7 had electrosorption capacities of 1.79 , 3.33, and 4.53 mg/g, respectively. The charge efficiencies were determined to be 0.15, 0.29, 0.46, and 0.43 for CNF, CNF-1:9, CNF-2:8, and CNF-3:7, respectively. The improved performance of the blend-based carbon nanofibers is attributable to the micro–mesoporous structure that was created during carbonization. The decrease in electrosorption capacity observed for CNF-3:7 in comparison to CNF-2:8 was attributed to the reduced specific surface area in the nanofibers possibly due to the fiber fusion and flattening that was observed from the SEM images. Also, the enlargement and merging of mesopores during carbonization at a higher CA proportion could have been a factor to the reduced capacity. Reduced specific surface area due to pore enlargement and merging of mesopores has been reported in other studies using different pore-forming agents (Lee *et al.* 2015).

A comparison of the desalination performance of the prepared carbon nanofibers with other works using carbon nanofibers from different precursors is given in Table 2. Relatively similar performance is noted for the electrodes prepared in this study with other porous carbon nanofiber-based electrodes that rely solely on the EDL mechanism for electrosorption.

Electrode cycling stability tests were performed on CNF-2:8 using NaCl solution with an initial concentration of 500 mg/L. The process involved repetitive electrosorption and desorption cycles using constant current with a terminal charging voltage of 1.2 and 0 V for discharging. For the cycles that were performed, the electrodes exhibited good cycling stability as shown in Figure S5. The electrodes had an electrosorption capacity of 5.83 mg/g after 35 cycles, indicating stable behavior.

To summarize, the properties of polymer-based carbon nanofiber electrodes for EDL-driven electrochemical applications need careful control during fabrication. The choice of precursors and their compositions significantly affect these properties. The suitable chemical properties of PAN for carbon fiber fabrication make it an ideal precursor, while green polymers such as CA are important to ameliorate functional properties. As demonstrated in this work, CA is a good enhancement agent to PAN-based carbon nanofibers. CA solution has excellent properties for electrospinning and helps reduce the total amount of PAN required during processing. However, the amount of CA that can be blended with PAN to produce good-quality carbon nanofiber sheets is limited by the carbonization conditions required for polymer-based precursors and the target pore structure of the end products. Significant thermal degradation of CA in blends with high CA % causes the end products to be too fragile for the intended application. Also, too high amounts of CA could lead to a diminished micro–mesopore structure and increased macro porosity due to higher burn-off of CA. Generally, for optimum performance, optimization of CA amount in PAN/CA blends is necessary, taking into consideration the ease of material processing, functional properties, and the intended applications.

Table 2 | Performance comparison of different carbon nanofiber-based electrodes

Precursor	CV electrolyte	Specific capacitance (F/g)	NaCl concentration (mg/L)	Cell voltage (V)	Salt removal (mg/g)	Ref.
PAN (CO_2 activated)	6 M KOH	228	192 μS/cm	1.6	4.64	Wang *et al.* (2012)
PAN/PMMA	1 M NaCl	53.6	500	1.2	5.61	Liu *et al.* (2016)
PAN/$DMSO_2$	1 M NaCl	42.7	500	1.2	8.1	Pan *et al.* (2015)
PVP/TiO_2	1 M NaCl	217	2,000	1.4	15.5	Guo *et al.* (2020)
PAN/NiO (HCl etching)	1 M NaCl	157.9	500	1.2	6.2	Hussain *et al.* (2018)
PAN/PVP (H_20 etching)	6 M KOH	202	100	1.2	6.51	Wang *et al.* (2016)
PAN/CA	6 M KOH	177.5	500	1.2	6.57	This work

CONCLUSIONS

In this work, micro/mesoporous carbon nanofibers were fabricated through electrospinning and subsequent stabilization and carbonization of a blend of PAN and CA at varying ratios. Among the electrodes that were compared, CNF-2:8 attained the highest specific surface area and pore volume that were, respectively, 2.8 times and 7.24 times higher than in plain CNF. Correspondingly, CNF-2:8 had the highest specific capacitance of 177.5 F/g, which was 36.1, 27.4, and 13.1% higher than those of CNF, CNF-1:9, and CNF-3:7, respectively, at a scan rate of 5 mV/s. In desalination, the electrosorption capacity was in the order CNF-2:8(6.57 mg/g) > CNF-3:7 (4.53 mg/g) > CNF-1:9 (3.33 mg/g) > CNF (1.79 mg/g). The optimum performance by CNF-2:8 was attributable to the high surface area and the combined microporous and mesoporous structure, which enhanced ion transfer, ion storage capacity, and access to electrosorption sites. In addition, the electrodes exhibited excellent cycling stability retaining ~90% of the initial capacity after multiple electrosorption/desorption cycles. The observed performance of the CA/PAN blend-based electrode demonstrates its high potential for application in desalination via CDI.

ACKNOWLEDGEMENT

This work was carried out with the financial support of the Partnership for Skills in Applied Sciences, Engineering and Technology (PASET) Regional Scholarship and Innovation Fund (RSIF), the International Centre of Insect Physiology and Ecology (ICIPE) – World Bank Financing Agreement No. D347-3A, and the World Bank – Korea Trust Fund Agreement No. TF0A8639 for PASET RSIF.

DATA AVAILABILITY STATEMENT

All relevant data are included in the paper or its Supplementary Information.

CONFLICT OF INTEREST

The authors declare there is no conflict.

REFERENCES

Ahdab, Y. D., Thiel, G. P., Böhlke, J. K., Stanton, J. & Lienhard, J. H. 2018 Minimum energy requirements for desalination of brackish groundwater in the United States with comparison to international datasets. *Water Res.* **141**, 387–404.

Ahmed, M. A. & Tewari, S. 2018 Capacitive deionization: Processes, materials and state of the technology. *J. Electroanal. Chem.* **813**, 178–192.

Al-Amshawee, S., Yunus, M. Y. B. M., Azoddein, A. A. M., Hassell, D. G., Dakhil, I. H. & Hasan, H. A. 2020 Electrodialysis desalination for water and wastewater: A review. *Chem. Eng. J.* **380**, 122231.

Alfredy, T., Jande, Y. A. C. & Pogrebnaya, T. 2019 Removal of lead ions from water by capacitive deionization electrode materials derived from chicken feathers. *J. Water Reuse Desalin.* **9** (3), 282–291.

Bai, X., Fu, R., Huang, W., Zhao, Y., Liu, B., Lin, S., Yan, B., Yang, Q. & Chen, S. 2022 Efficient and recyclable ultra-thin diameter polyacrylonitrile nanofiber membrane: Selective adsorption of cationic dyes. *Sep. Purif. Technol.* **302**, 122109.

Barua, B. & Saha, M. C. 2018 Studies of reaction mechanisms during stabilization of electrospun polyacrylonitrile carbon nanofibers. *Polym. Eng. Sci.* **58** (8), 1315–1321.

Brogioli, D., La Mantia, F. & Yip, N. Y. 2018 Thermodynamic analysis and energy efficiency of thermal desalination processes. *Desalination* **428**, 29–39.

Cychosz, K. A. & Thommes, M. 2018 Progress in the physisorption characterization of nanoporous gas storage materials. *Engineering* **4** (4), 559–566.

Dadol, G. C., Lim, K. J. A., Cabatingan, L. K. & Tan, N. P. B. 2020 Solution blow spinning–polyacrylonitrile–assisted cellulose acetate nanofiber membrane. *Nanotechnology* **31** (34), 345602.

Donnet, J. B., Bahl, O. P., Bansal, R. C. & Wang, T. K., 2003 *Encyclopedia of Physical Science and Technology*, 3rd edn. (Meyers, R. A., ed.). Academic Press, New York, pp. 431–455.

Ekabutr, P., Ariyathanakul, T., Chaiyo, S., Niamlang, P., Rattanaveeranon, S., Chailapakul, O. & Supaphol, P. 2018 Carbonized electrospun polyvinylpyrrolidone/metal hybrid nanofiber composites for electrochemical applications. *J. Appl. Polym. Sci.* **135** (1), 45639.

El-Deen, A. G., Barakat, N. A. M., Khalil, K. A. & Kim, H. Y. 2013 Development of multi-channel carbon nanofibers as effective electrosorptive electrodes for a capacitive deionization process. *J. Mater. Chem. A* **1** (36), 11001–11010.

Elisadiki, J., Jande, Y. A. C., Kibona, T. E. & Machunda, R. L. 2020 Highly porous biomass-based capacitive deionization electrodes for water defluoridation. *Ionics* **26** (5), 2477–2492.

Erdmann, R., Kabasci, S. & Heim, H.-P. 2021 Thermal properties of plasticized cellulose acetate and its β-relaxation phenomenon. *Polymers* **13** (9), 1356.

Fan, Q., Ma, C., Wu, L., Wei, C., Wang, H., Song, Y. & Shi, J. 2019 Preparation of cellulose acetate derived carbon nanofibers by $zncl_2$ activation as a supercapacitor electrode. *RSC Adv.* **9** (12), 6419–6428.

Feng, Q., Wu, D., Zhao, Y., Wei, A., Wei, Q. & Fong, H. 2018 Electrospun AOPAN/RC blend nanofiber membrane for efficient removal of heavy metal ions from water. *J. Hazard. Mater.* **344**, 819–828.

Gaan, S., Mauclaire, L., Rupper, P., Salimova, V., Tran, T.-T. & Heuberger, M. 2011 Thermal degradation of cellulose acetate in presence of bis-phosphoramidates. *J. Anal. Appl. Pyrolysis* **90** (1), 33–41.

Ganster, J. & Fink, H.-P. 2013 Cellulose and Cellulose Acetate. In: *Bio-Based Plastics*, S. Kabasci (Ed.), John Wiley & Sons, Chichester, United Kingdom, pp. 35–62.

García-Mateos, F. J., Ruiz-Rosas, R., María Rosas, J., Morallón, E., Cazorla-Amorós, D., Rodríguez-Mirasol, J. & Cordero, T. 2020 Activation of electrospun lignin-based carbon fibers and their performance as self-standing supercapacitor electrodes. *Sep. Purif. Technol.* **241**, 116724.

Ghosh, S., Yong, W. D., Jin, E. M., Polaki, S. R., Jeong, S. M. & Jun, H. 2019 Mesoporous carbon nanofiber engineered for improved supercapacitor performance. *Korean J. Chem. Eng.* **36** (2), 312–320.

Guo, L., Ding, M., Yan, D., Pam, M. E., Vafakhah, S., Gu, C., Zhang, W., Valdivia y Alvarado, P., Shi, Y. & Yang, H. Y. 2020 High speed capacitive deionization system with flow-through electrodes. *Desalination* **496**, 114750.

Hussain, T., Wang, Y., Xiong, Z., Yang, J., Xie, Z. & Liu, J. 2018 Fabrication of electrospun trace NiO-doped hierarchical porous carbon nanofiber electrode for capacitive deionization. *J. Colloid Interface Sci.* **532**, 343–351.

Jo, E., Yeo, J.-G., Kim, D. K., Oh, J. S. & Hong, C. K. 2014 Preparation of well-controlled porous carbon nanofiber materials by varying the compatibility of polymer blends. *Polym. Int.* **63** (8), 1471–1477.

Ju, Y.-W., Park, S.-H., Jung, H.-R. & Lee, W.-J. 2009 Electrospun activated carbon nanofibers electrodes based on polymer blends. *J. Electrochem. Soc.* **156** (6), A489.

Khodayari, P., Jalilian, N., Ebrahimzadeh, H. & Amini, S. 2022 Electrospun cellulose acetate/polyacrylonitrile/thymol/Mg-metal organic framework nanofibers as efficient sorbent for pipette-tip micro-solid phase extraction of anti-cancer drugs. *React. Funct. Polym.* **173**, 105217.

Kim, B. K., Oh, Y. S., Lee, Y. M., Yoon, L. K. & Lee, S. 2000 Modified polyacrylonitrile blends with cellulose acetate: Blend properties. *Polymer* **41** (1), 385–390.

Kim, D.-W., Kil, H.-S., Nakabayashi, K., Yoon, S.-H. & Miyawaki, J. 2017 Structural elucidation of physical and chemical activation mechanisms based on the microdomain structure model. *Carbon* **114**, 98–105.

Kim, J.-G., Kim, H.-C., Kim, N. D. & Khil, M.-S. 2020 N-doped hierarchical porous hollow carbon nanofibers based on PAN/PVP@SAN structure for high performance supercapacitor. *Compos. Part B: Eng.* **186**, 107825.

Kumar, S., Rath, T., Mahaling, R. N. & Das, C. K. 2007 Processing and characterization of carbon nanofiber/syndiotactic polystyrene composites in the absence and presence of liquid crystalline polymer. *Compos. Part A: Appl. Sci. Manufact.* **38** (5), 1304–1317.

Lee, H.-M., Kim, H.-G., Kang, S.-J., Park, S.-J., An, K.-H. & Kim, B.-J. 2015 Effects of pore structures on electrochemical behaviors of polyacrylonitrile (PAN)-based activated carbon nanofibers. *J. Ind. Eng. Chem.* **21**, 736–740.

Liu, J., Xiong, Z., Wang, S., Cai, W., Yang, J. & Zhang, H. 2016 Structure and electrochemistry comparison of electrospun porous carbon nanofibers for capacitive deionization. *Electrochim. Acta* **210**, 171–180.

Liu, X., Liu, H., Mi, M., Kong, W., Ge, Y. & Hu, J. 2019 Nitrogen-doped hierarchical porous carbon aerogel for high-performance capacitive deionization. *Sep. Purif. Technol.* **224**, 44–50.

Liu, X., Shanbhag, S., Bartholomew, T. V., Whitacre, J. F. & Mauter, M. S. 2021 Cost comparison of capacitive deionization and reverse osmosis for brackish water desalination. *ACS ES&T Eng.* **1** (2), 261–273.

Ma, C., Wu, L., Dirican, M., Cheng, H., Li, J., Song, Y., Shi, J. & Zhang, X. 2021 ZnO-assisted synthesis of lignin-based ultra-fine microporous carbon nanofibers for supercapacitors. *J. Colloid. Interface Sci.* **586**, 412–422.

Myint, M. T. Z. & Dutta, J. 2012 Fabrication of zinc oxide nanorods modified activated carbon cloth electrode for desalination of brackish water using capacitive deionization approach. *Desalination* **305**, 24–30.

Nataraj, S. K., Yang, K. S. & Aminabhavi, T. M. 2012 Polyacrylonitrile-based nanofibers – A state-of-the-art review. *Prog. Polym. Sci.* **37** (3), 487–513.

Nie, C., Pan, L., Li, H., Chen, T., Lu, T. & Sun, Z. 2012 Electrophoretic deposition of carbon nanotubes film electrodes for capacitive deionization. *J. Electroanal. Chem.* **666**, 85–88.

Nie, P., Wang, S., Shang, X., Hu, B., Huang, M., Yang, J. & Liu, J. 2021 Self-supporting porous carbon nanofibers with opposite surface charges for high-performance inverted capacitive deionization. *Desalination* **520**, 115340.

Pan, H., Yang, J., Wang, S., Xiong, Z., Cai, W. & Liu, J. 2015 Facile fabrication of porous carbon nanofibers by electrospun PAN/dimethyl sulfone for capacitive deionization. *J. Mater. Chem. A* **3** (26), 13827–13834.

Peng, W., Wang, W., Han, G., Huang, Y. & Zhang, Y. 2020 Fabrication of 3D flower-like MoS_2/graphene composite as high-performance electrode for capacitive deionization. *Desalination* **473**, 114191.

Phan, D.-N., Lee, H., Huang, B., Mukai, Y. & Kim, I.-S. 2019 Fabrication of electrospun chitosan/cellulose nanofibers having adsorption property with enhanced mechanical property. *Cellulose* **26** (3), 1781–1793.

Porada, S., Weinstein, L., Dash, R., van der Wal, A., Bryjak, M., Gogotsi, Y. & Biesheuvel, P. M. 2012 Water desalination using capacitive deionization with microporous carbon electrodes. *ACS Appl. Mater. Interfaces* **4** (3), 1194–1199.

Porada, S., Zhao, R., van der Wal, A., Presser, V. & Biesheuvel, P. M. 2013 Review on the science and technology of water desalination by capacitive deionization. *Prog. Mater Sci.* **58** (8), 1388–1442.

Qasim, M., Badrelzaman, M., Darwish, N. N., Darwish, N. A. & Hilal, N. 2019 Reverse osmosis desalination: A state-of-the-art review. *Desalination* **459**, 59–104.

Shui, P. & Alhseinat, E. 2020 Quantitative insight into the effect of ions size and electrodes pores on capacitive deionization performance. *Electrochim. Acta* **329**, 135176.

Suss, M. E., Porada, S., Sun, X., Biesheuvel, P. M., Yoon, J. & Presser, V. 2015 Water desalination via capacitive deionization: What is it and what can we expect from it? *Energy Environ. Sci.* **8** (8), 2296–2319.

Tarus, B. K., Jande, Y. A. C. & Njau, K. N. 2022 Electrospun carbon nanofibers for use in the capacitive desalination of water. *New Carbon Mater.* **37** (6), 1066–1084.

Tong, Y., Zhou, S., Zhou, J., Zhang, G., Li, X., Zhao, C. & Liu, P. 2021 Advances in efficient desalination technology of capacitive deionization for water recycling. *J. Water Reuse Desalin.* **11** (2), 189–200.

Voutchkov, N. 2018 Membrane Desalination - Process Selection, Design, and Implementation. In: *Sustainable Desalination Handbook*, Gude, V. G. (ed.), Butterworth-Heinemann, Oxford, United Kingdom, pp. 3–24.

Wang, G., Pan, C., Wang, L., Dong, Q., Yu, C., Zhao, Z. & Qiu, J. 2012 Activated carbon nanofiber webs made by electrospinning for capacitive deionization. *Electrochim. Acta.* **69**, 65–70.

Wang, G., Qian, B., Wang, Y., Dong, Q., Zhan, F. & Qiu, J. 2016 Electrospun porous hierarchical carbon nanofibers with tailored structures for supercapacitors and capacitive deionization. *New J. Chem.* **40** (4), 3786–3792.

Wang, D., Yue, Y., Wang, Q., Cheng, W. & Han, G. 2020 Preparation of cellulose acetate-polyacrylonitrile composite nanofibers by multi-fluid mixing electrospinning method: Morphology, wettability, and mechanical properties. *Appl. Surf. Sci.* **510**, 145462.

Wu, Y.-B., Bi, J., Lou, T., Song, T.-B. & Yu, H.-Q. 2015 Preparation of a novel PAN/cellulose acetate-Ag based activated carbon nanofiber and its adsorption performance for low-concentration SO_2. *Int. J. Miner. Metall. Mater.* **22** (4), 437–445.

Xu, W., Xin, B. & Yang, X. 2020 Carbonization of electrospun polyacrylonitrile (PAN)/cellulose nanofibril (CNF) hybrid membranes and its mechanism. *Cellulose* **27** (7), 3789–3804.

Xue, J., Wu, T., Dai, Y. & Xia, Y. 2019 Electrospinning and electrospun nanofibers: Methods, materials, and applications. *Chem. Rev. (Washington, DC, U. S.)* **119** (8), 5298–5415.

Yan, J., Xiao, W., Chen, L., Wu, Z., Gao, J. & Xue, H. 2021 Superhydrophilic carbon nanofiber membrane with a hierarchically macro/meso porous structure for high performance solar steam generators. *Desalination* **516**, 115224.

Yin, J., Zhang, W., Alhebshi, N. A., Salah, N. & Alshareef, H. N. 2020 Synthesis strategies of porous carbon for supercapacitor applications. *Small Methods* **4** (3), 1900853.

Zhang, L., Aboagye, A., Kelkar, A., Lai, C. & Fong, H. 2014 A review: Carbon nanofibers from electrospun polyacrylonitrile and their applications. *J. Mater. Sci.* **49** (2), 463–480.

Zhang, B., Kang, F., Tarascon, J.-M. & Kim, J.-K. 2016 Recent advances in electrospun carbon nanofibers and their application in electrochemical energy storage. *Prog. Mater Sci.* **76**, 319–380.

Zhang, Y., Chen, L., Mao, S., Sun, Z., Song, Y. & Zhao, R. 2019 Fabrication of porous graphene electrodes via CO_2 activation for the enhancement of capacitive deionization. *J. Colloid. Interface Sci.* **536**, 252–260.

First received 14 April 2023; accepted in revised form 11 December 2023. Available online 21 December 2023